Numerical models of lithospheric deformation forming the Southern Alps of New Zealand

Muriel Gerbault,[1] Stuart Henrys, and Fred Davey
Geological and Nuclear Sciences, Lower Hutt, New Zealand

Received 14 December 2001; revised 19 December 2002; accepted 17 March 2003; published XX Month 2003.

[1] Compression of the entire continental lithosphere is considered using two-dimensional numerical models to study the influence of the lithospheric mantle on the geometry of continental collision in its initial stages. The numerical scheme incorporates brittle-elastic-ductile rheology, heat transfer, surface processes, and fault localization. Models are based on the central section of the New Zealand Southern Alps, where continental collision has occurred along the Alpine Fault since about 7 Ma. The results are compared to the surface relief, the GPS convergence velocity, the measured electrical conductivity, and the geometry of the crustal root imaged from seismic velocity measurements. The crustal deformation is characterized by localized uplift at the plate boundary (Alpine Fault) and by two secondary zones of faulting. One is located ~60–80 km east of the Alpine Fault, at the start of upper crust bending (or tilting), and the other is located ~100–130 km east of the Alpine Fault as a result of shear strain propagating to the surface through the ductile lower crust. The observed asymmetric shape of the crustal root is best reproduced for mantle lithosphere strength of the order of 200 MPa and an intermediate rate of strain softening. A lower strength of the mantle lithosphere can produce symmetric thickening, but the amplitude of the crustal root is too small when compared to observations. The observed 20 km offset between the maximum in surface relief and the crustal root was not satisfactorily reproduced. This offset is most likely due to the three dimensionality of oblique collision in the Southern Alps. *INDEX TERMS:* 3902 Mineral Physics: Creep and deformation; 8102 Tectonophysics: Continental contractional orogenic belts; 8120 Tectonophysics: Dynamics of lithosphere and mantle—general; 8159 Tectonophysics: Rheology—crust and lithosphere; 9355 Information Related to Geographic Region: Pacific Ocean; *KEYWORDS:* mechanical modeling, rheology of the lithosphere, strain localization, decoupled crust and mantle, continental collision, Southern Alps

Citation: Gerbault, M., S. Henrys, and F. Davey, Numerical models of lithospheric deformation forming the Southern Alps of New Zealand, *J. Geophys. Res.*, *108*(0), XXXX, doi:10.1029/2001JB001716, 2003.

1. Introduction

[2] The South Island of New Zealand provides a simple setting in which geodynamic models of active convergent mountain belts can be compared to observations. The Australian/Pacific plate boundary through the South Island has progressively formed about 45 Ma, transforming an initial Eocene passive margin into the dextral strike-slip Alpine fault, with ~450 km of offset [*Wellman and Willet*, 1942; *Carter and Norris*, 1976; *Sutherland et al.*, 2000]. Oblique convergence commenced about 7 Ma and has resulted in ~100 km of shortening and the uplift of the Southern Alps mountain range [*Wellman*, 1979; *DeMets et al.*, 1990; *Beavan and Haines*, 2001] (Figure 1).

[3] In regions of oblique relative plate motion and where both shear and compressive deformation occur together, two-dimensional (2-D) models [e.g., *Willett*, 1999; *Batt and Braun*, 1999] can help understand which deformation structures are due solely to the compressive component of the system. *Koons* [1990] and *Beaumont et al.* [1996] first applied such models to the Southern Alps of New Zealand. They identified that the parameters that control the large-scale geometry of the orogen are a combination of crustal rheological properties, surface processes, and boundary conditions applied at the base of the crust. However, these models assume that the Pacific crust is driven by lithospheric mantle against the Australian lithosphere, so that an imposed basal velocity discontinuity (commonly referred to as the "S point") controls the location of deformation. Modeling of the interaction between the crust and the mantle lithosphere is biased by this prescribed discontinuous boundary condition. During the mountain building process, deflection of the Moho should also be constrained by the ability of the underlying mantle lithosphere to deform. In this paper we incorporate the

[1]Now at Institut de Recherche pour le Développement, Université Paul Sabatier, Toulouse, France.

0148-0227/03/2001JB001716$09.00

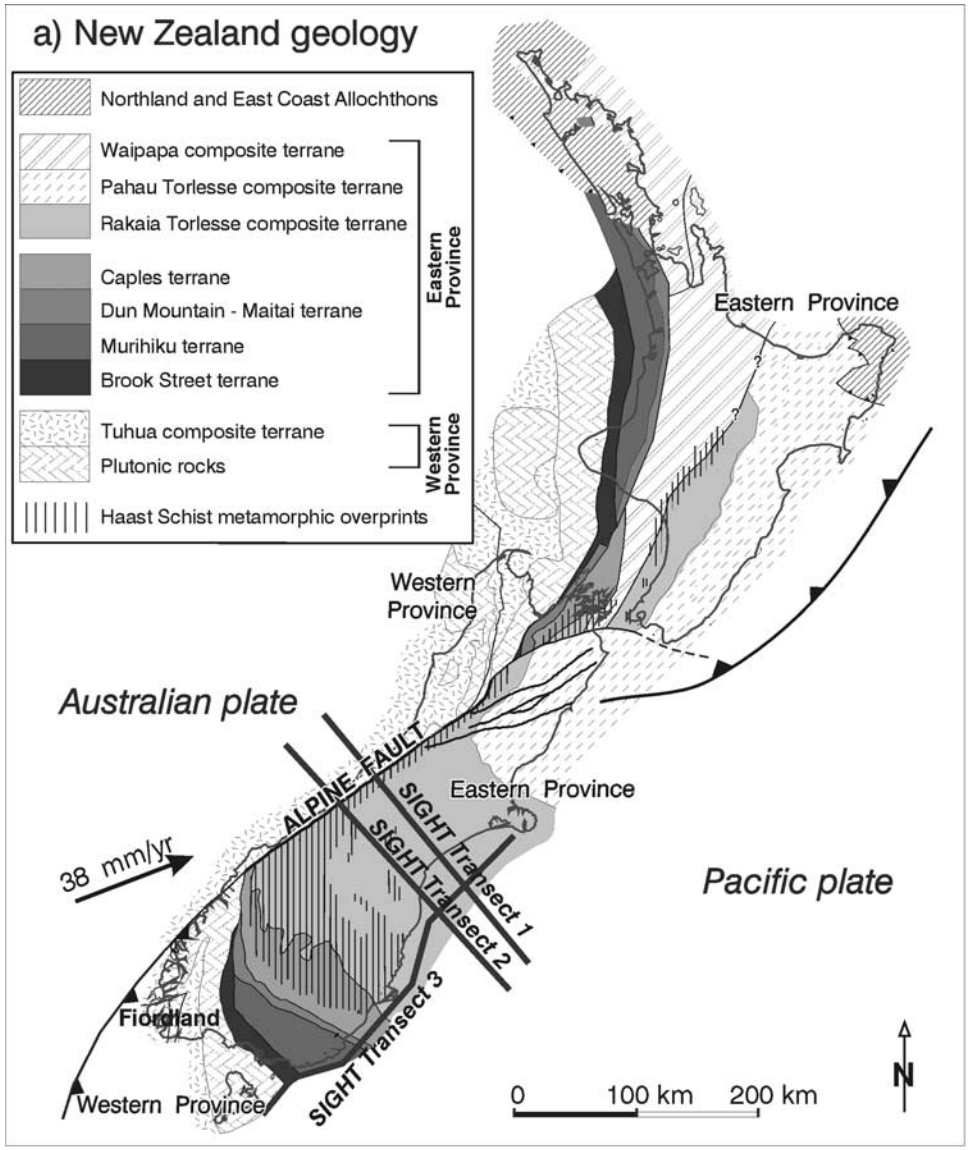

Figure 1. (a) Geological setting in the Southern Alps of New Zealand [*Mortimer*, 2000]: Eastern Province terranes on the Pacific plate deform against Western Province terranes. Dark gray lines show approximate location of geophysical transects for the SIGHT experiment. (b) Seismic velocity model across SIGHT line 2 from *Scherwath et al.* [1998]. Note that horizontal coordinates do not coincide with the following model coordinates. Vertical exaggeration is 4.

mantle lithosphere when examining the growth of the Southern Alps.

[4] The lithospheric mantle can undergo tectonic shortening in three principal ways: homogeneous shortening by distributed thickening, folding (or buckling) by subperiodical bending of competent lithospheric layers, or intracontinental subduction by asymmetric underthrusting of one block under the other along a major shear zone. While the occurrence of symmetric or asymmetric mantle thickening is an old debate [*Houseman et al.*, 1981; *Mattauer*, 1986], it is only recently that large-scale folding is understood to be a primary response of the lithosphere to induced compressional stress [e.g., *Martinod and Davy*, 1992; *Burov et al.*, 1993; *Gerbault et al.*, 1999; *Cloetingh et al.*, 1999]. Lithospheric folding develops due to its strength contrast with low-viscosity asthenosphere and evolves as a single megafold where rheological weaknesses concentrate [*Burg and Podladchikov*, 1999; *Cloetingh et al.*, 1999].

[5] At the timescale of 10–20 Myr, symmetric downwelling of the mantle lithosphere may also result from a convective or a Rayleigh-Taylor instability, due to cold and dense thickening mantle lithosphere [e.g., *Houseman et al.*, 1981]. This mechanism has been proposed for the Southern Alps of New Zealand to explain the observed negative gravity anomaly and *P* wave delays [*Stern*, 1995; *Molnar et al.*, 1999; *Stern et al.*, 2000]. Using large-scale models that include the lithosphere and upper mantle, *Pysklywec et al.* [2000] showed that a Rayleigh-Taylor-type instability or asymmetric intracontinental subduction can evolve into dripping or slab break off of the mantle lithosphere, depending on the rate of convergence, the density distribution, and the strength of the mantle lithosphere.

[6] In contrast to the approach of *Pysklywec et al.* [2000], we investigate the smaller-scale deformation within the lithosphere. We incorporate preexisting heterogeneities based on known rheological discontinuities (terranes of different tectonic history, Figure 1a). For example, the Alpine Fault is a major strike-slip feature that has been in existence for ~45 Myr prior to the actual compressional episode [*Sutherland et al.*, 2000], and we model it as an initial vertical zone of weakness. Since we ask how the strength contrasts determine the asymmetry of the lithospheric mantle and its effects on crustal deformation, our formulation of the initial state of the plate boundary is intermediate between two opposing approaches. One end-member assumes complete stress and deformation discontinuity across a narrow zone (the S point models are related to this approach), and the other end-member accounts for lateral continuity of stresses across the plate boundary and allows for lithospheric-scale folding. We performed a series of model calculations to examine the mechanical properties of the lithosphere (on geological timescales) that give rise to the present Southern Alps. Instead of presenting an exhaustive set of results, several new geophysical observations allow us to confine the range of numerical parameters and therefore constrain model calculations. The most important data sets we choose to compare models to are the present surface elevation, mapped faults, contemporary GPS measurements, the image of the crustal root deduced from seismic velocity modeling [*Scherwath et al.*, 1998] (Figure 1b), gravity and magnetotelluric observations, and the distribution of earthquakes. In this paper we demonstrate how a well-constrained numerical model can bring insight into the development of a young continental collision zone such as the New Zealand Southern Alps.

2. Numerical Modeling

2.1. Numerical Approach

2.1.1 General Features

[7] We use the mixed finite element-finite difference code Parovoz [*Poliakov and Podladchikov*, 1992]. It is based on the fast Lagrangian analysis continuum method (FLAC [*Cundall and Board*, 1988]), which incorporates an explicit time-marching scheme, and allows the use of a wide range of constitutive laws such as brittle-elastic-ductile rheology derived by rock experimentalists [e.g., *Brace and Kohlstedt*, 1980; *Ranalli*, 1995]. Parovoz handles initiation and propagation of nonpredefined faults (shear bands). The present version also includes diffusive surface processes, heat advection and conduction including initial age-dependent temperature field. This code has proved efficient in modeling many tectonic features, such as salt diapirism [*Poliakov and Podladchikov*, 1992], lithospheric folding [*Gerbault et al.*, 1999], lithospheric rifting [*Buck and Poliakov*, 1998; *Burov and Poliakov*, 2001]. More details are given in Appendix A concerning the numerical method, calculation of the geotherm, and rheological laws.

[8] The lithosphere is modeled as a medium of 300 by 30 quadrilateral elements, with a total length of 600 km and depth of 60 km (Figure 2). Both lateral borders are free to slip vertically, the left border is fixed in the horizontal direction and a velocity $V_x = 4.5 \times 10^{-10}$ m s^{-1} (15 mm yr^{-1}) is applied on the right border. The lithosphere floats on the asthenosphere within the gravity field; hydrostatic boundary conditions are applied at the bottom of the model, with an underlying density of 3250 kg m^{-3}. The surface is stress free.

[9] An initial temperature distribution is calculated, which includes a thermomechanical age dependency, analogous to that of oceanic lithospheres, and incorporates crustal radioactive heat [*Burov and Diament*, 1995] (see Appendix A). A thermomechanical age equal to 100 Ma is assigned here, based on the last episode of extension that affected the New Zealand shelf [*Laird*, 1993] and was likely to have rejuvenated most of the lithosphere.

[10] The model lithospheric plate is divided into areas of different mechanical properties (Table 1). The initial crustal thickness, or the depth to the Moho, is set at 25 km; this choice is constrained by several observations from seismological studies, indicating a "far-field" crustal thickness of 22–26 km [*Scherwath et al.*, 1998; *Godfrey et al.*, 2001]. The density distribution is 2650, 2900, and 3200 kg m^{-3}, respectively for the first 19 km, from 19 to 25 km, and from 25 to 60 km depth.

2.2. Rheology

[11] Elastic-viscous-brittle behavior is modeled with a pressure-dependent Coulomb criterion for brittle failure, and a temperature-dependent creep power law for ductile behavior (see Table 1 and Appendix A). For each element of the model and at any time step, if the shear stress provided by the creep law reaches the Mohr-Coulomb plastic yield, then

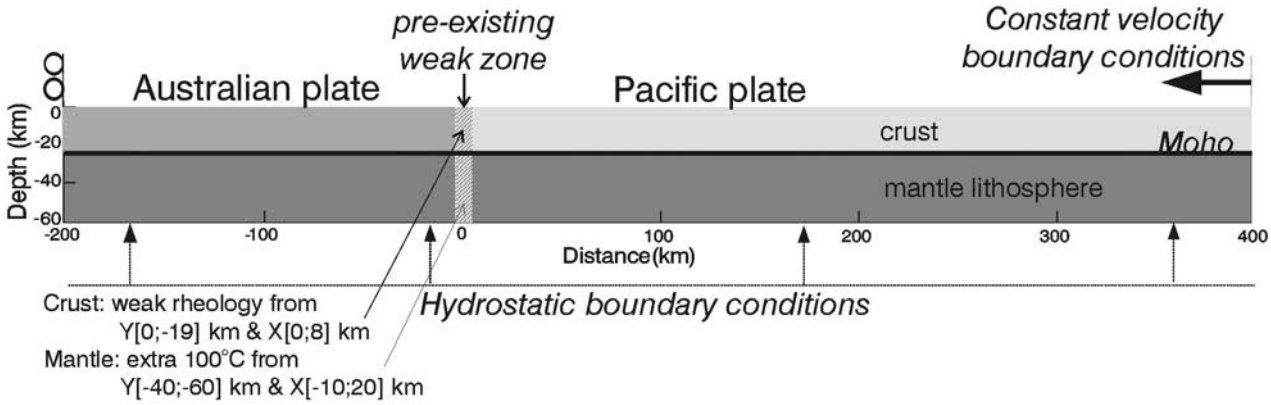

Figure 2. Initial conditions for the 2-D model (see text).

nonassociative failure occurs. In this sense, the brittle-ductile transition is self-consistently defined in the modeling.

[12] Above the Moho, a vertical division separates the Australian crust, to the left (west) from the Pacific crust to the right (east). The "Australian crust" and "Pacific crust" rheologies are based on geological mapping and petrology of basement terranes (Figure 1a) and regional geophysical data. The Australian crust is composed of Paleozoic plutonic rocks (Western Province) that are found in northwest South Island, in Fiordland, and offshore on the Challenger and Campbell Plateaus (Figure 1a). There is no evidence for internal deformation in the Australian lithosphere, apart from a broad flexural bending toward the Alpine Fault [*Sircompe and Kamp*, 1998]. Power law creep parameters for the Australian crust are thus chosen so that the lower crust remains elastobrittle (Table 1). East of the Alpine Fault, the Eastern Province rocks are composed of low-grade metasediments (graywacke to schist) that were accreted in Mesozoic times. These rocks are younger than the Western Province rocks, and are likely to be mechanically weaker. A dominant quartzite rheology (Table 1) best matches the observed geology, the seismological brittle-ductile transition at 12 km [*Leitner et al.*, 2001], the convergence rate, and constraints on the geotherm.

[13] In between the Australian and Pacific crust, a zone of weakness is inserted (four elements wide and located at $X = [0; 10]$ km) and simulates the Alpine Fault (Figure 2). Inclusion of a preexisting fault zone derives from the observation that Neogene plate boundary deformation along the Alpine Fault is most likely an inherited Eocene older structure [*Sutherland et al.*, 2000]. If this preexisting fault zone is not present, then a folding instability develops in the Pacific crust. The strength (or viscosity) contrast between the brittle crust and the deeper ductile crust only needs to be of ~3 orders of magnitude for folding to develop after ~5% of homogeneous shortening [e.g., *Bull et al.*, 1992; *Burov and Diament*, 1995; *Gerbault et al.*, 1999].

[14] Below the Moho, dry olivine is assumed to control the strength of the mantle lithosphere (see creep law parameters in Table 1). Strain softening is included, with details in Appendix A: its effects are discussed later in the paper. A zone of weakness must also be inserted in the mantle else periodic undulations develop, due to periodic folding of the "strong" mantle lithosphere. Preliminary numerical tests show that both assumptions of a preexisting zone of weak rheology or a preexisting thermal perturbation lead to similar results. Since a thermal anomaly would better correspond to extra heat present at depth due to sustained shear along the trend of the Alpine Fault, a perturbation of 100°C is inserted below the crustal weak zone, at $X = [-10; +20]$ km and $Y = [-40; -60]$ km.

Table 1. Rheological Properties for Reference Model[a]

Layers	Creep Law	Power n	Constant A, Pa^{-n} s^{-1}	Activation Energy Q, J mol^{-1}	Mohr-Coulomb Brittle properties	Friction/Viscosity Softening Rates
Mantle lithosphere	olivine	3	7×10^4	5.2×10^5	S_o = 200 MPa → 50 MPa $\phi = 0°$	$\varepsilon_s = 0.1 \rightarrow 1.$
Australian crust	olivine				$\phi = 30° \rightarrow 10°$ S_o = 20 MPa	$\varepsilon_s = 0.1 \rightarrow 1.$
Lower crust					S_o = 200 MPa, $\phi = 0°$	no softening
Pacific crust	wet quartzite	2.3	3.2×10^{-4}	1.54×10^5	$\phi = 30°$, S_o = 20 MPa	$\varepsilon_s = 0.1 \rightarrow 2$: $\mu = \mu/10$
Lower crust						no softening
Weak zone crust	wet granite	1.9	2×10^{-4}	1.37×10^5	S_o = 20 MPa, $\phi = 15°$, $\lambda = 0.33$	$\varepsilon_s = 0.1 \rightarrow 2$: $\mu = \mu/10$
Lower crust						no softening
Sediments and top 3 km Austral. crust	wet granite				S_o = 20 MPa, $\phi = 15°$, $\lambda = 0.33$	no softening

[a]Power law creep parameters are from *Ranalli* [1995]. Mohr-Coulomb parameters are cohesion So, friction angle ϕ, and fluid pressure ratio λ (normal stress proportional to lithostatic pressure). Strain softening acts within both given values of the total shear strain, and modifies the value located on the same line in the previous column. Where specified, strain softening acts instead on viscosity μ.

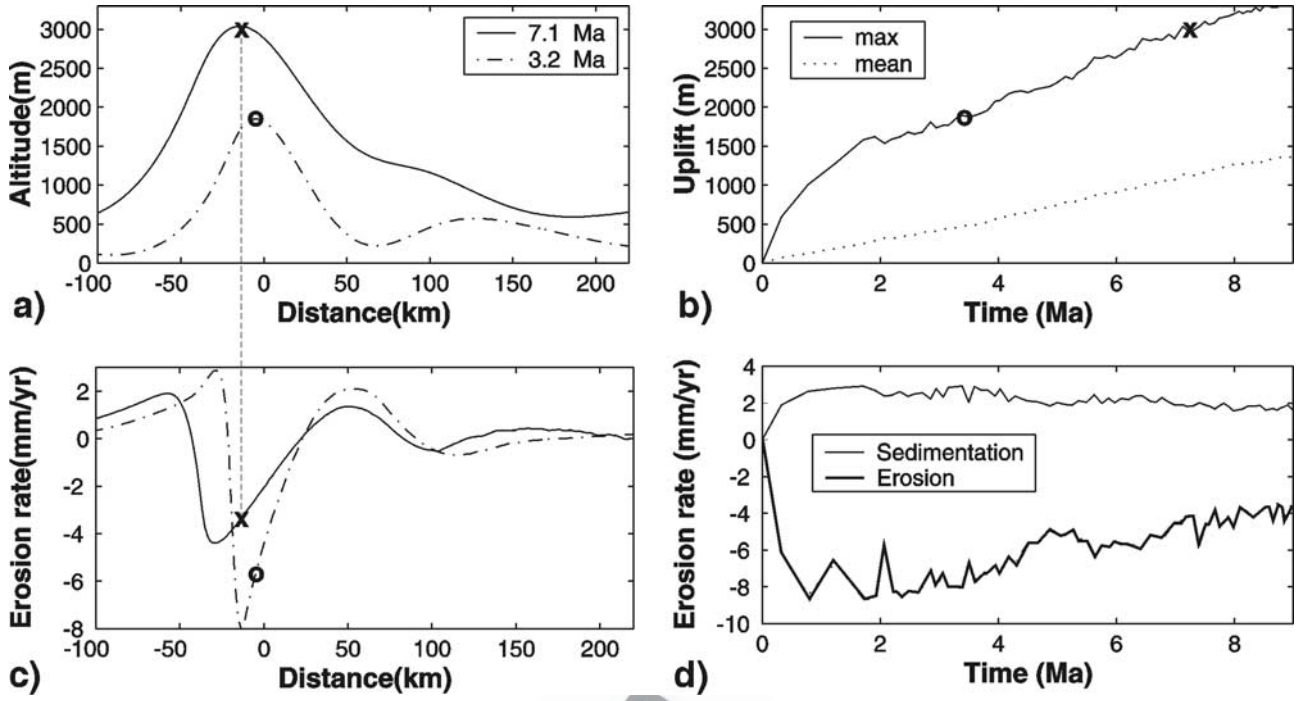

Figure 3. Surface deformation for reference model: (a and b) topography and (c and d) erosion rates plotted against horizontal distance (Figures 3a and 3c) and time (Figures 3b and 3d). Circles and crosses correspond to the spatial maximum of topography after 3.2 and 7 Myr. After 7 Myr this maximum is located ~15 km east from the maximum erosion rate.

[15] Results after 7 Myr of shortening are presented in Figures 3 and 4for the reference model. In Figures 3 and 4, the origin of the horizontal axis ($X = 0$) is located at the initial preexisting crustal weak zone. Comparisons with electrical conductivity, geodesy, seismic Moho, and gravity anomaly are shown in Figures 5, 6, and 7. The following sections discuss deformation in the crust, the role of lithospheric mantle strength on the geometry of the orogen, and the relative position of the maximum topography and the crustal root, compared to observations across the Southern Alps. The discussion also includes additional models that use a number of supplementary parameters. The results and comments on these models in relation to the reference model are summarized in Table 2.

3. Deformation in the Crust

3.1. Surface Uplift

[16] Surface deformation is displayed through time in Figure 3. Maximum elevation develops above the initial weak zone (at $X = 0$), evolves 10 km toward the west, and reaches ~3000 m within 7 Myr (Figure 3a). A secondary maximum develops close to $X = 100$ km (this position reduces as time progresses).

[17] The whole lithosphere is affected by a component of regional surface uplift (Figure 3b), due to homogeneous thickening. This regional or mean surface uplift (different from rock exhumation) is around 0.15 mm yr^{-1}, with a maximum of 5 mm yr^{-1} (3000 m in 7 Myr, Figures 3a and 3b), with respect to the initial zero level. The mean density of the lithosphere is likely to increases with increasing distance away from the South Island as the lithospheric rock composition becomes more similar to oceanic lithosphere. Therefore our model cannot fit real far-field surface elevations, because such lateral density contrasts are not taken into account. Homogeneous thickening is the change in shape of a layer that is compressed horizontally and thickens vertically due to mass conservation. Homogeneous (or uniform) thickening is primarily, a fundamental way to accommodate lithosphere compression and is complementary to localized deformation and mountain growth. It occurs as a consequence of elastic and viscous rheologies, and also diffuse faulting [*Bull et al.*, 1992; *Martinod and Davy*, 1992; *Burov et al.*, 1993; *Burg and Podladchikov*, 1999; *Gerbault*, 2000]. Although uniform shortening is generally difficult to quantify from the geology because of its continuous character, vertically elongated structures in the lower crust exhumed at the Alpine Fault are interpreted by *Little et al.* [2001] as markers of uniform shortening that develops at least 100 km east from the plate boundary. Furthermore, GPS and shear wave splitting data show evidence for "distributed deformation" [e.g., *Moore et al.*, 2002, and references therein].

[18] The maximum erosion rate is located ~10 km west of the maximum of the topography (Figure 3c). It reaches a quasi-stable value of ~5 mm yr^{-1} after 2 Myr (Figure 3d). The sedimentation rate is lower than the erosion rate, partly because of the open mass flow condition at the borders of the model and partly because of the numerical approximation of sedimentation (see Appendix A).

[19] Sediment budget studies [e.g., *Griffiths and McSaveney*, 1983; *Adams and Gabites*, 1985] and cooling ages [*Tippett and Kamp*, 1993] both indicate that uplift rates increase exponentially up to ~10 mm yr^{-1} at the Alpine

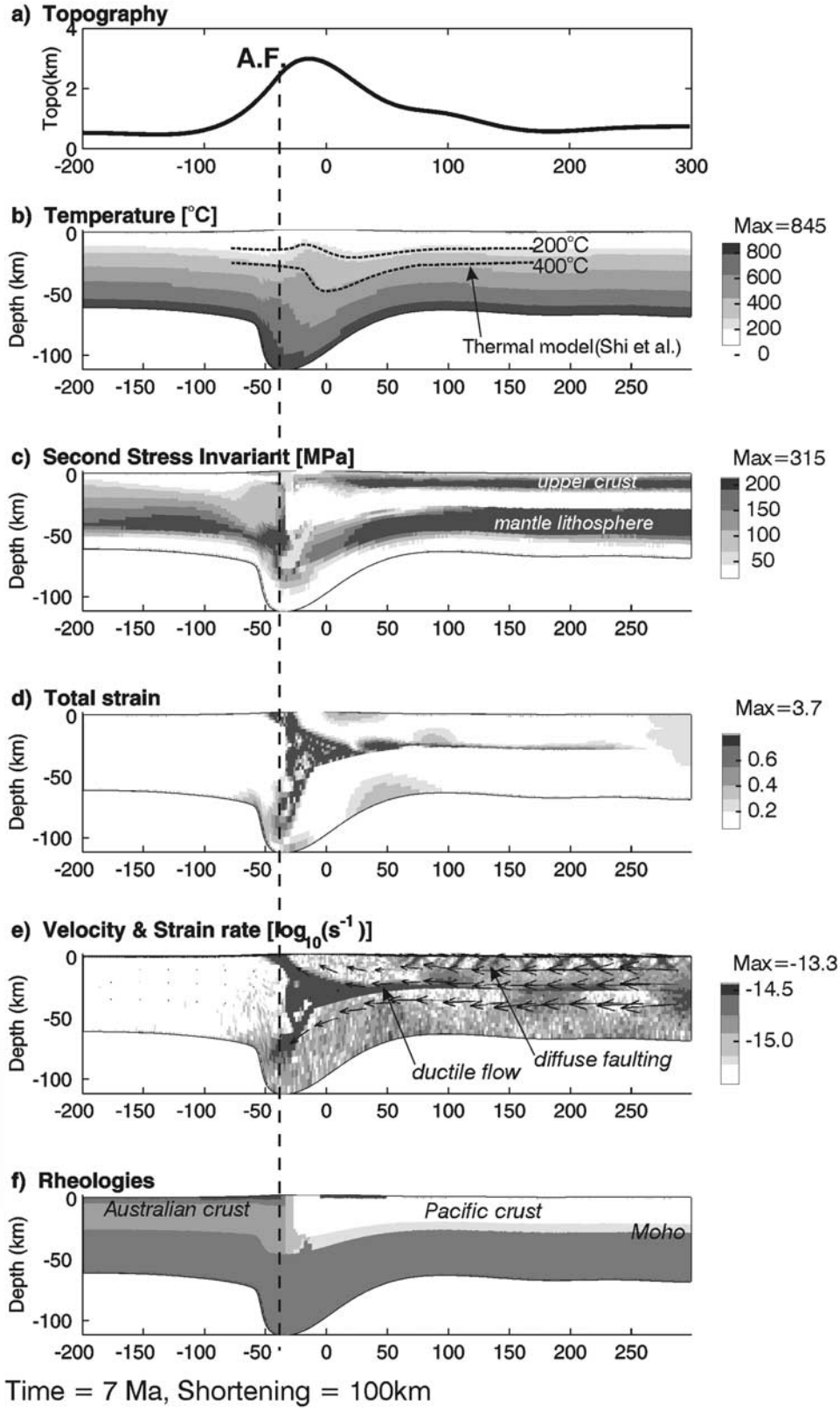

Figure 4. Reference model after 7 Myr of shortening (100 km). A.F. is Alpine Fault. (a) Surface topography, (b) temperature field, (c) deviatoric shear stress, (d) total shear strain (elastic, viscous and brittle), (e) shear strain rate and instantaneous velocity vectors, and (f) rheological phases (layers). Dark elements close to the surface are sediments. The vertical dashed line is positioned with reference to Figure 4e shear zone rising to the surface, namely, which we call the Alpine Fault zone.

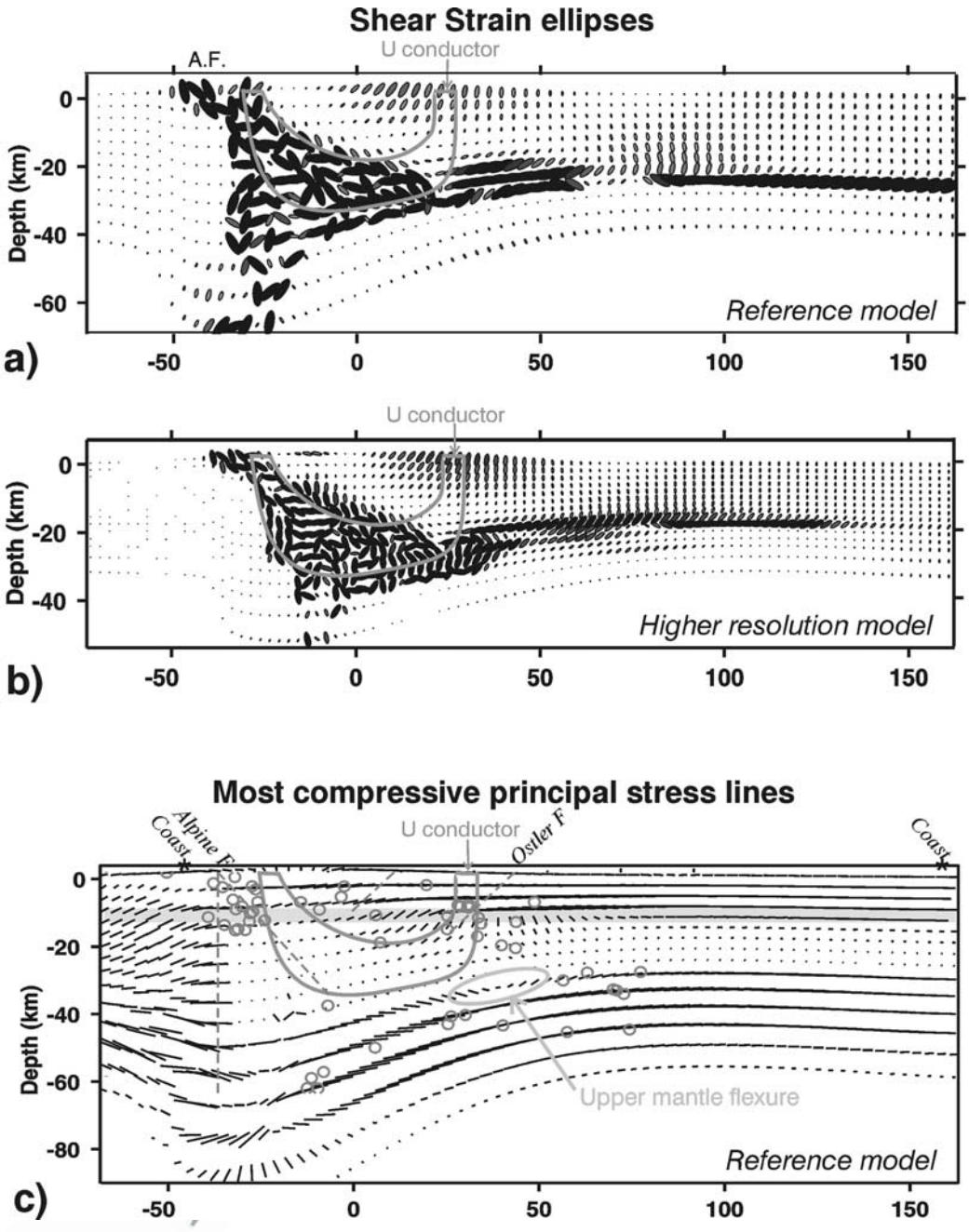

Figure 5. Shear strain ellipses after 7 Myr. (a) Reference model. Numerical values of the shear strain are same as for Figure 4d. (b) Higher-resolution model (400 × 40 elements). Superimposition of the high electrical conductivity signal in thick gray contour: note the ''flip'' of shear strain ellipses in the ductile lower crust, at $X \sim 25$ km. (c) Most compressive principal stress lines for the reference model. Gray circles are earthquakes distribution, dashed lines are presumed geometry of faults at depth, and thick gray line is the 12 km deep seismogenic zone (all data from *Leitner et al.* [2001]).

Fault. There is also an indication for the initiation of rapid erosion in the Southern Alps beginning at 2–3 Ma [*Tippett and Kamp*, 1993]. *Koons* [1989, 1990] studied the role of asymmetric erosion and recognized that rapid removal of material from the West Coast controls the asymmetry of deformation on either side of the Main Divide, a point developed also by *Beaumont et al.* [1992, 1996].

[20] The factor of 2 difference in the erosion rate between our models and the observations is due to surface processes being modeled with a numerical algorithm that smoothes surface deformation. This is also the reason why fluvial transport is not incorporated in the modeling, as developed by *Koons* [1990] and *Beaumont et al.* [1992, 1996].

3.2. Temperature, Strain, and Stress Distribution

[21] Figure 4b displays the deflection of initially horizontal isotherms after 7 Myr of shortening. Isotherms are elevated in the upper crustal area just east of the modeled

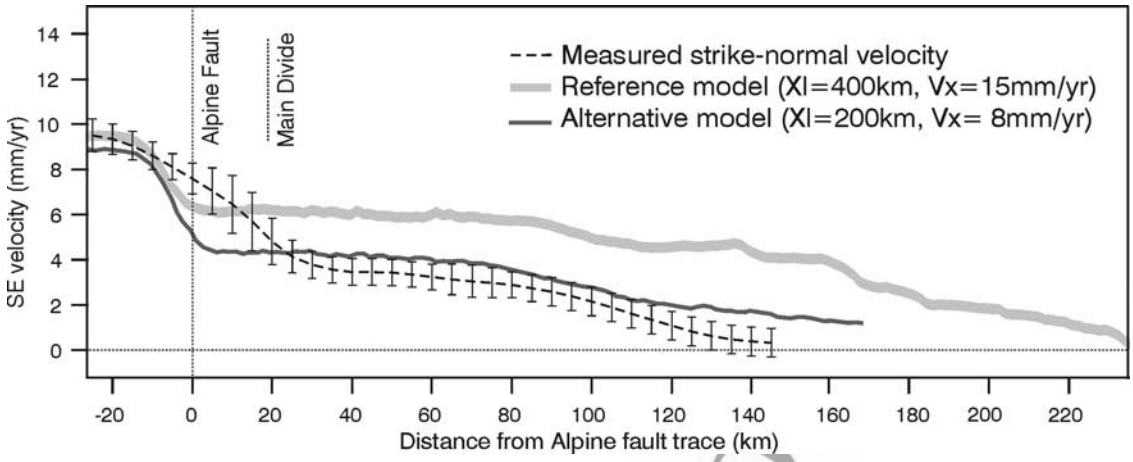

Figure 6. Comparison of surface convergence velocity with GPS measurements [*Beavan and Haines*, 2001]. Thick light gray line is the reference model, with distance from the plate boundary to the eastern border of the model X_l = 400 km, and applied convergence rate V_x = 15 mm yr^{-1}. Thin dark gray line is an alternative model with smaller distance X_l = 200 km and slower convergence rate V_x = 8 mm yr^{-1}. Note the difference in velocity increase at the Alpine Fault, and the similar change in slope at a distance of ~80 km to the east.

"Alpine Fault zone" (see vertical dashed line referring to its modeled position on Figure 4). They are deflected downward at midcrustal depths. This geometry is very similar to results obtained from previous thermal modeling [*Shi et al.*, 1996] (dashed lines on Figure 4b), which was compared to heat flow measurements. This supports the fact that advection is the main mode of heat transfer as a response to 7 Myr of compression.

[22] Figure 4c displays distribution of the shear stress $\sigma_s = [(\sigma_{xx} - \sigma_{yy})^2/2 + \sigma_{xy}^2]^{1/2}$. One can identify three strong layers: the Australian lithosphere, the Pacific upper crust, and the Pacific lithospheric mantle. Note the geometry of weak zones that develop in the center of the model, at the plate boundary.

[23] Figure 4d displays the accumulated total shear strain $\varepsilon_s = [(\varepsilon_{xx} - \varepsilon_{yy})^2/2 + \varepsilon_{xy}^2]^{1/2}$, with time, while Figure 4e displays the instantaneous shear strain rate and instantaneous velocity vectors. Deformation accumulates in a "crustal root", which progressively increases in width and depth. Low-strength Pacific material accumulates against the Australian lithosphere, connecting (1) the Alpine Fault zone in the upper crust, emerging to the surface at $X \sim -30$ km, (2) a horizontal shear zone in the ductile lower crust, extending toward the east, and (3) a "west dipping" shear zone propagating downward into the lithospheric mantle.

3.3. Shear Strain Localization: The Alpine Fault

[24] The Alpine Fault shear zone develops at the site of the initial vertical weak zone in the crust. This active zone progressively inclines and propagates into the Australian crust and toward the surface (compare Figure 4e with inclined shear zone and Figure 4f, which shows rheological layers and vertical initial plate boundary zone). Its geometry is determined by two conditions: (1) the preexisting vertical weak zone and (2) the development of a shear zone inclined between 30° and 45° from the maximum principal strain and principal stress orientation (nonassociated plasticity with friction angle ϕ = 30° and dilatation angle ψ = 0° [*Vermeer*, 1990; *Gerbault et al.*, 1998]).

[25] The Alpine Fault shear zone is wider than the mapped fault: the numerical model produces shear bands that occupy a width of about five numerical elements. Since the present model deals with 2 km wide elements, the modeled Alpine Fault zone is thus 10 km wide. Because the initial vertical weak zone is not in the "correct" orientation to accommodate thrust faulting inclined at 30°–45°, the active shear zone is superimposed only on part of the initial weak zone: this superimposition (Figures 4d and 4f) occurs around 10–15 km depth, where the shear strength is highest with depth, but lowest in horizontal direction. This geometry is logical if one considers how a fault would develop according to minimized energy patterns.

[26] The present-day transform shear zone corresponds to the active shear zone in the model, after 7 Myr, and not to the initial vertical weak zone. While 2-D modeling cannot address the issue of strain partitioning, 3-D modeling [*Gerbault et al.*, 2002] also indicates a progressive inclination with time of the vertical plate boundary, along which transcurrent shear occurs. This is consistent with indications of nonpartitioned strain in the Southern Alps [e.g., *Braun and Beaumont*, 1995].

3.4. Shear Strain Localization: General Features

[27] The modeled Alpine Fault shear zone curves at depth to merge with a ductile shear zone in the lower crust (Figures 4d and 4e). At this level, deformation propagates to the east, within the ~10 km thick low-viscosity lower crust, and allows the upper crust to detach from the lithospheric mantle. In section 4, we illustrate how the eastern tip of this lower crust ductile shear zone can propagate via upper crustal faulting to the surface, at a characteristic distance ranging from 100 to 130 km from the Alpine Fault shear zone.

[28] In contrast to the development of localized shear strain at the Alpine Fault zone, diffuse faulting in the brittle upper crust is represented numerically by conjugate shear bands alternating in both dip directions in time and space

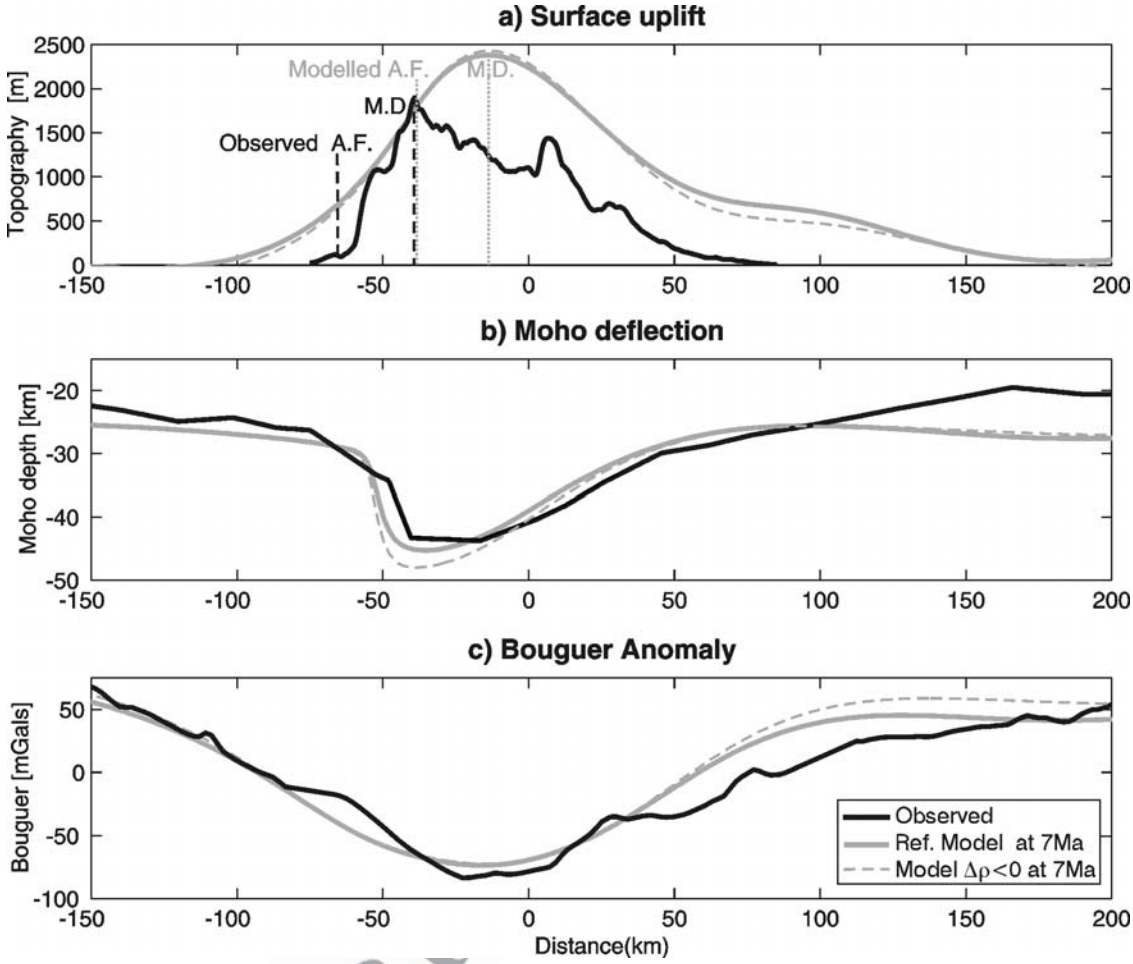

Figure 7. Comparisons of reference model with observed (a) topography, (b) Moho, and (c) gravity anomaly. Black lines are observed topography, Moho from seismic velocity models along transect 2 [*Scherwath*, 2001], and measured Bouguer gravity anomaly. Gray lines are same horizons obtained with the reference model. Dashed gray lines are an additional model with a density of 3300 kg m^{-3} for the mantle lithosphere and basal hydrostatic compensation of 3250 kg m^{-3}. In Figure 7a, vertical dashed lines are the observed (in black) and modeled (in gray) positions of the Alpine Fault (A.F.) and of the main divide (M.D.). Five hundred meters have been subtracted from the model topography (Figure 7a), and 100 mGal have been added to the model gravity (Figure 7c) (see text for justification).

t2.1 **Table 2.** Summary of Numerical Models Illustrated in This Paper[a]

t2.2 Models	Model-Associated Figures	Characteristics	General Results
t2.3 Reference model	Figures 3, 4, 5, 6, 7	k_{er} = 1000 m^2 yr^{-1}	highest surface relief to the west.
t2.4		mantle strength So = 200 MPa	crustal root depth of 45 km
t2.5		softening rate $\varepsilon_s = 0.1 \rightarrow 1$.	subducting mantle lithosphere to the west
t2.6		density contrast 3250/3200	higher horizontal velocity than GPS
t2.7		length = 600 km, V_x = 15 mm yr^{-1}	
t2.8 GPS modeling	Figure 4	length = 400 km, V_x = 8 mm yr^{-1}	crustal root depth of 40 km
t2.9			matches GPS horizontal velocity
t2.10 Gravity modeling	Figure 7	density contrast 3300/3250	no significant difference to reference model
t2.11			gravity anomaly too small
t2.12 Low strength	Figure 8a	mantle strength S_o = 50 MPa	low symmetric surface relief
t2.13			crustal root depth of 35 km
t2.14			subducting mantle lithosphere to the east
t2.15 Low strength	Figure 8b	k_{er} = 500 m^2 yr^{-1}	low symmetrical surface relief
t2.16 plus rapid softening		mantle strength S_o = 50 MPa	crustal root depth of 35 km
t2.17 plus low erosion		softening rate $\varepsilon_s = 0.05 \rightarrow 0.5$	symmetric thickening of mantle lithosphere
t2.18 Slow strain softening	Figure 9	mantle strength S_o = 200 MPa	two topographic highs
t2.19		softening rate $\varepsilon_s = 0.1 \rightarrow 2$	subducting mantle lithosphere to the west

t2.20 [a]Models characteristics and results are described in terms of changes from the first reference model.

(Figure 4e). This model behavior may correspond to the abundant reactivated faults observed within the Torlesse graywackes east of the Alpine Fault [*Oliver and Keene*, 1990; *Cox and Findlay*, 1995; *Long et al.*, 2003].

[29] Figure 5a displays the shear strain using ellipses where each ellipse represents how an initially perfect circle is deformed through time. Darkest ellipses are those that undergo the most shear strain (same shading distribution as Figure 4d). Figure 5b shows shear strain ellipse representation for a model identical to the reference model, but using a more refined grid (400 × 40 elements). A higher resolution allows us to reproduce a narrower Alpine Fault zone and examine lower crustal deformation in more detail.

[30] In the crustal root, progressive rotation of the high-strain ellipses demonstrates how the Pacific crust diverges in response to indentation by the Australian plate (the sharp western border of high strain ellipses coincides with rheological discontinuities inserted in the model). The Alpine Fault zone consists of multiple ellipse directions, associated with thickening of the crust, and fault shearing (Figure 5).

[31] Inclined ellipses located at the base of the lower crust suggest that mantle lithosphere drives material from beneath the crustal root. This shows that although a uniform velocity is applied at the east end of the model, the mantle and the crust move with different rates with respect to each other from ~130 km east of the plate boundary (Figure 5).

[32] In the lower crust at about $X \sim 25$ km, 60 km east of the plate boundary, the shear orientation of ellipses shifts, with locally a horizontal orientation corresponding to less horizontal compression. Above, brittle deformation accumulates in the upper crust, in a zone located ~60 km east from the Alpine Fault zone: it is the resulting of uplift of the upper crust, as it is tilted (or flexed), and dragged with the ductile lower crust (Figures 4d and 5). Tilting and flexure of the upper crust are consistent with the fan shape of geological strain markers [*Little et al.*, 2001].

3.5. Modeled Strain, Observed Faults, and Electrical Conductivity in the Southern Alps

[33] The localization of high strain ~60–80 km southeast of the Alpine Fault (Figure 5) is in very good agreement with a series of active structures, the Lake Heron-Forest Creek Faults and the Irishman Creek Fault, which are structurally similar faults that dip either east or west [*Beanland*, 1987; *Oliver and Keene*, 1990; *Woodward et al.*, 1994]. This characteristic distance also coincides with the eastern edge of the Bouguer gravity anomaly.

[34] Electrical resistivity models derived from a magnetotelluric profile experiment show a U-shaped high-conductivity structure under the Southern Alps [*Wannamaker et al.*, 2002]. The lowest resistivities (40–100 ohm m^{-1}) lie at 25–30 km depth below the surface (Figure 5) and extend upward as narrow near-vertical conductors near the Alpine Fault trace and 60–70 km to the east. This latter branch of the conductor appears to coincide with fault zones (the Forest Creek-Lake Heron Faults), which would allow deep crustal fluids to migrate to the surface [*Templeton et al.*, 1998]. Among the deformation mechanisms that are expected to operate in lower crustal ductile rocks, diffusion creep may dominate when the volume of fluids is small (<0.5 vol %), and under relatively low stress conditions [*Tullis and Yund*, 1991]. *Wannamaker et al.* [2002] discuss the cause of the high conductivity in the crust and favor the presence of interconnected fluids resulting from prograde metamorphic reactions occurring in the crustal root. Excess water is likely to lead to increased fluid pressure. High pore pressure is also inferred to be the origin of a low *P* wave velocities [*Stern et al.*, 2001; *Eberhart-Phillips and Bannister*, 2002] that are coincident with the high-conductivity structure.

[35] In the present numerical models, we have not accounted for the presence of fluids being produced and evolving with time. However, the coincidence of the shape of the high-conductivity zone with the area of high strain (Figure 5b) suggests a link between conductivity and fluids as an image of the high shear zones in the crust. The change in ellipse orientations at about $X = 25$ km, is interpreted as a zone of less compression due to clockwise bending of the upper crust to the west, and in which interconnected fluids may accumulate.

[36] Figure 5c represents stress lines, each line showing the local orientation of the most compressive stress. Figure 5c suggests that the conductivity signal is caused by internal crustal deformation mechanisms, because it is located above and to the west of the change in stress orientation corresponding to extensional flexure of the upper mantle. Earthquakes superimposed on our 2-D model [*Leitner et al.*, 2001] show good agreement with areas of enhanced compression and also seem to coincide with local stress orientation changes but, at the same time, surround the zone of inferred high pore fluids.

3.6. Comparison to Contemporary Plate Motion and Width of the Orogen

[37] Figure 6 displays a comparison between the observed GPS convergence velocity and the result from the model. This modeled convergence velocity is evaluated after ~7 Myr of shortening, for one time step, which is typically of the order of 30 years. We see that the reference model has a generally higher convergence rate than observations (thick light gray line on Figure 6). This is because the reference model is defined to be extending for 400 km east of the plate boundary, and to have a convergence rate of 15 mm yr^{-1}. These values were used, first, to avoid numerical border effects on the resulting deformation and, second, to match plate tectonic models that indicate ~100 km of convergence within 7 Myr. Present convergent rates based on GPS observations [*Beavan and Haines*, 2001], however, record a velocity of ~8 mm yr^{-1}, as measured across the width of the South Island (200 km), over a 10 year time period. We also plotted the resulting velocity for an alternative model, in which the distance from the border of the model to the plate boundary has been reduced to 200 km and a convergence rate of 8 mm yr^{-1} has been imposed (Table 2). After 7 Myr, the crust and mantle deformation from this alternative model are similar to those from the reference model, except that the crustal root is less deep, since the shortening rate is slower. Comparison of the surface velocity with the GPS data is now more consistent (thin dark gray line on Figure 6).

[38] Two interesting features are noticable on Figure 6: First, we note a similar stabilization of convergence velocity, in the data and in the models, at ~80–100 km from the Alpine Fault; this feature can be related to the area where the crust detaches from the mantle lithosphere. Second, the

extent of increasing convergence velocity at the Alpine Fault is broader in the data than in the model. This is due to elastic strain accumulating from the last earthquake cycle, and we would expect the velocity increase, over time, to become sharper in GPS measurements and thus more similar to the models.

[39] About 100 km east of the Alpine Fault in the central Southern Alps, the topography increases to ~1500 m. Many strike-slip and reverse faults coexist in this area. Previous analytic, analog and numerical models also reproduce this zone of secondary surface uplift, which represents conjugate brittle shear with respect to the Alpine fault, i.e., the other edge of the double-vergent wedge characteristic of orogenic process [*Koons*, 1990; *Koons and Henderson*, 1995; *Beaumont et al.*, 1996]. Our models emphasize that the amplitude of this secondary zone of uplift depends on a number of parameters. First, erosion and sedimentation processes are known to help localize deformation [*Beaumont et al.*, 1996]. If surface processes are imposed slowly, deformation is less asymmetric and diffuses over a broader area, to the east in the case of the Southern Alps. Second, if the lower crust is assumed to be relatively stronger than in the reference model, then ductile shear deformation is confined to a smaller depth range, and tends to propagate more to the east, in order to occupy the same volume. If the Moho is chosen initially deeper (say at 30 km), then the distance at which this secondary uplift occurs increases. Finally, a strong mantle lithosphere also contributes to producing wider surface deformation. This is discussed in section 4.

4. Deformation in the Lithospheric Mantle

4.1. Observations of Deformation at and Under the Moho in the Southern Alps

[40] Seismic velocity models [*Davey et al.*, 1998; *Scherwath et al.*, 2000; *Eberhart-Phillips and Bannister*, 2002] provide an image of a crustal root ~100 km wide, with a maximum depth of 40–45 km, and increasing southward between transect 1 and transect 2 (Figures 1a and 1b). The deepest part of the crust lies ~20 km east from the Main Divide (itself ~20 km east from the Alpine Fault). The thickness and location of the crustal root indicate that the orogen is overcompensated and is marked by large negative (−30 mGal) isostatic gravity anomalies [*Woodward*, 1979].

[41] *Stern* [1995] first proposed an elastic flexure model where a subducting mantle lithosphere body 100 km wide and centered at 120 km depth (density contrast +30 kg m^{-3}) was able to match both the observed amplitude and wavelength of observed Bouguer gravity data (−100 mGal). Support for the existence a cold subducting mantle is found in teleseismic *P* waves arrivals recorded on two dense profiles across the Southern Alps [*Stern et al.*, 2000]. To match the observed 1 s advance in *P* wave travel times, recorded from three teleseismic earthquakes, requires a high-speed body (up 7% velocity perturbation) extending to over 160 km depth. Using a larger set of teleseims, *Kohler and Eberhart-Phillips* [2002] are able to map a similar west dipping high-velocity sheet that varies from 60 to 100 km in width and extends to ~180 km depth with a maximum 3% perturbation. Furthermore, a few well-located mantle earthquakes have been recorded beneath the central Southern Alps at depths from 25 to 60 km deep (shown in Figure 5c) [*Reyners*, 1987]. They correspond to the faster portion of the high-velocity zone determined from teleseismic *P* wave travel time inversion [*Kohler and Eberhart-Phillips*, 2002].

[42] In section 4.2 we compare our "reference" model to the observed topography and Moho in the Southern Alps. In section 4.3 we discuss the role of lithospheric mantle rheology, using additional models that were modified from the reference model (Table 2).

4.2. Comparison to the Seismic Moho and Gravity

[43] Figure 7 shows comparisons of the model and observed surface topography (Figure 7a) and Moho (Figure 7b) across the Southern Alps. Since our models do not account for progressive change in lithospheric rock composition, away from the plate boundary, we are unable to match these boundaries in the far field. Indeed, the modeled topography is consistently higher than observed since uniform uplift acts in our model by raising the entire surface. Since the base level of topography corresponds to a regional value, in isostatic equilibrium, the data in Figure 7a therefore have 500 m subtracted so that far-field data are at mean sea level

[44] The resultant Moho wavelength and depth are a good match to the shape of the crustal root (Figure 7b) derived from ray trace modeling. However, the model shows no significant offset between maximum topography and deepest portion of the crustal root. In the present reference model, it is even slightly to the east of the crustal root, but in alternative models (not shown) with a slightly weaker Australian upper crust, we obtain a maximum topography located ~10 km west of the crustal root. The cause for this discrepancy of offset in the model, when compared to observations is further discussed in section 4.6.

[45] Figure 7c shows the comparison between observed and modeled gravity anomaly. The detail of gravity calculation is given in Appendix A. One hundred milligals were added to the overall modeled anomaly, which is again justified by the fact that the modeled far field is in isostatic equilibrium. The geodynamic models do not include preexisting basins or paleobathymetry in the initial set up. Therefore the comparison between the model gravity and observed data does not match to the east of the central gravity low, where the anomaly, owing to the presence of a thick Cenozoic sedimentary basin [*Field and Browne*, 1989], is greatest. The mismatch in detail to the west of the crustal root is most likely due to density variations in the Australian crust.

[46] The density contrast (300 kg m^{-3}) at the Moho contributes to ~50% to the negative gravity anomaly, and the upper and lower crust density contrast (250 kg m^{-3}) contributes ~30%. The reference model (gray line) has a positive density contrast (50 kg m^{-3}) across the lithosphere-asthenosphere boundary that contributes a small (<10 mGal) long-wavelength (>200 km) component to the gravity anomaly. Figure 7c also shows an additional model in which hydrostatic compensation at the base of the model is handled with a negative density contrast. In this model the colder mantle lithosphere is assigned a density of 3300 kg m^{-3}, and Archimede's force acts with a density equal to 3250 kg m^{-3}. Results from this model (dashed line in Figure 7c) show that the Moho is deeper, by ~5 km, compared to Moho observed

by seismic velocity modeling, while the wavelength and maximum amplitude of Bouguer anomaly remain the same as our reference model. These results suggest that a 10–20% change of density at the lithosphere-asthenosphere boundary is not diagnostic in fitting the observed gravity anomaly. While density distribution at depths of transition from the lithosphere to the asthenosphere remains difficult to resolve with seismological data [e.g., *Karato*, 1993; *Ishii and Tromp*, 1999; *Sabadini et al.*, 2002], our result supports the assumption of gravity modeling studies that use a constant density distribution at these depths (e.g., *Vacher and Souriau* [2001] for the Pyrenees).

[47] On the other hand, the lithospheric root calculated from our modeling (center of mass at 80 km depth) is smaller than that delineated by *Stern et al.* [2000]. An accurate comparison with this work would require a test of the dependency of density (and viscosity) on both increasing temperature and pressure with deforming mantle lithosphere. If we are to model accurately the dynamics of the lithosphere-asthenosphere in the Southern Alps, then the depth of our modeling needs to be increased to 120 km, and how compression applies down to such depth should also be questioned. This additional modeling is beyond the scope of this paper where we have chosen to focus on deformation of the crust and mantle lithosphere.

4.3. Remarks on the Rheology of the Lithospheric Mantle

[48] Lateral density contrasts and the geometry of rheological boundaries between the Australian and Pacific plates can clearly be a first-order cause of the direction of "mantle subduction" in the Southern Alps of New Zealand. However, the mantle's strength and rate of strain softening are also first-order controls on the geometry of mantle lithosphere thickening, as recently illustrated by *Pysklywec et al.* [2000].

[49] There are several ways in which the strength of the mantle lithosphere can vary. For example, a warmer geotherm tends to induce lower viscosity, due to the temperature-dependent power law constitutive behavior. Parameters of the power law may vary when extrapolated to real mantle depths, and other mechanisms of deformation than dislocation creep may even dominate [*Karato*, 1993] (see review by *Ranalli* [1995]). The choice of dry versus wet olivine creep parameters modifies the depth of the brittle-ductile transition in the mantle lithosphere [e.g., *Rannalli*, 1995; *Pysklywec et al.*, 2002], and thus the thickness of its strong layer and, consequently, the length scale of mantle deflection are modified. As a consequence of the large uncertainties in a realistic constitutive law for the mantle lithosphere, and after having tested about 300 models, we choose to demonstrate the control of strength and strain softening in a simple manner. Regardless of which mechanism controls the strength of the mantle lithosphere in detail, since maximum strength is bounded by both friction and cohesion, we prescribe zero friction and vary the cohesion (see Table 1). However, this cohesion should not be considered as a physical cohesive value for rocks.

4.4. Effect of Lithospheric Mantle's Strength and Symmetry of its Deformation

[50] From a mechanical point of view, Moho topography (i.e., wavelength and amplitude) is dependent on the ability of mantle lithosphere to deform. The stronger the lithospheric mantle (either viscous or brittle), the easier it is to deflect because it can support large internal stress contrasts responding to lateral loading. This is similar to the mechanism of lithospheric folding [e.g., *Gerbault et al.*, 1999], in which the strong mantle lithosphere (dark layer in Figure 4c) can buckle "plastically" with a wavelength proportional to ~4–6 times its thickness, and an amplitude proportional to its strength ratio with the surrounding layers. In contrast, a mantle with relatively low viscosity deforms by uniform viscous thickening. In this case the amplitude of localized deformation is diminished, so that the crust is less affected by deformation in the mantle.

[51] Models were produced for mantle lithosphere strength of 500 MPa (not shown). As expected, broad flexure of the mantle lithosphere leads to broad surface deformation. The secondary maximum of topography, mentioned previously, tends to develop more easily, as it coincides with flexural uplift of the mantle lithosphere.

[52] Figure 8 displays two models with an initial mantle strength of 50 MPa, which reduces to 20 MPa by strain softening (Table 2). In the first model (Figure 8a), the "Australian" mantle underthrusts the "Pacific" mantle after 7 Myr of convergence. In the second model (Figure 8b), in which the rate of strain softening has been increased and the coefficient of erosion reduced (see Figure 8 caption for values), two conjugate shear zones develop so that mantle deformation remains symmetric. These models show that in case the mantle lithosphere has a low strength (of the order of magnitude of cohesion, 20 MPa), then the stress magnitude involved in lithospheric deformation compete with stresses due to mass transfer at the surface. This is understandable given the unpredictability of preferential movement along two conjugate thrust faults, which results from local equilibrium in mass transfer along vertical columns. However, none of our models with initial mantle strength of 50 MPa allow for a large width and amplitude of crustal thickening because there is insufficient build up of stress to support significant mantle lithosphere deflection. Models with an initial mantle strength of 50 MPa produce a crustal root ~50 km wide and <35 km deep, in contrast to models with an initial strength >200 MPa, in which "Pacific plate" subduction always develops.

[53] In our models, (a)symmetry of the crustal root develops associated with (a)symmetry of entire lithospheric thickening. The symmetrical deformation of Figure 8b is in agreement with indications from *P* wave delays for symmetric lithospheric thickening. However, the significantly smaller shape of the Moho renders this model unsatisfactory. More complex constitutive laws, such as temperature-dependent strain softening [*Zhang et al.*, 2000], may be required in order to reproduce asymmetric crustal root and symmetric mantle lithosphere thickening, as indicated by teleseismic arrivals across the Southern Alps [*Stern et al.*, 2000].

4.5. Effect of Strain Softening

[54] Our models, together with other studies [*Pysklywec et al.*, 2000; *Huismans and Beaumont*, 2002], show that if strain softening is too rapid, deformation remains localized over a narrower region than indicated by observations from the Southern Alps. An extreme situation is that deformation remains concentrated in the initial vertical zones of weak-

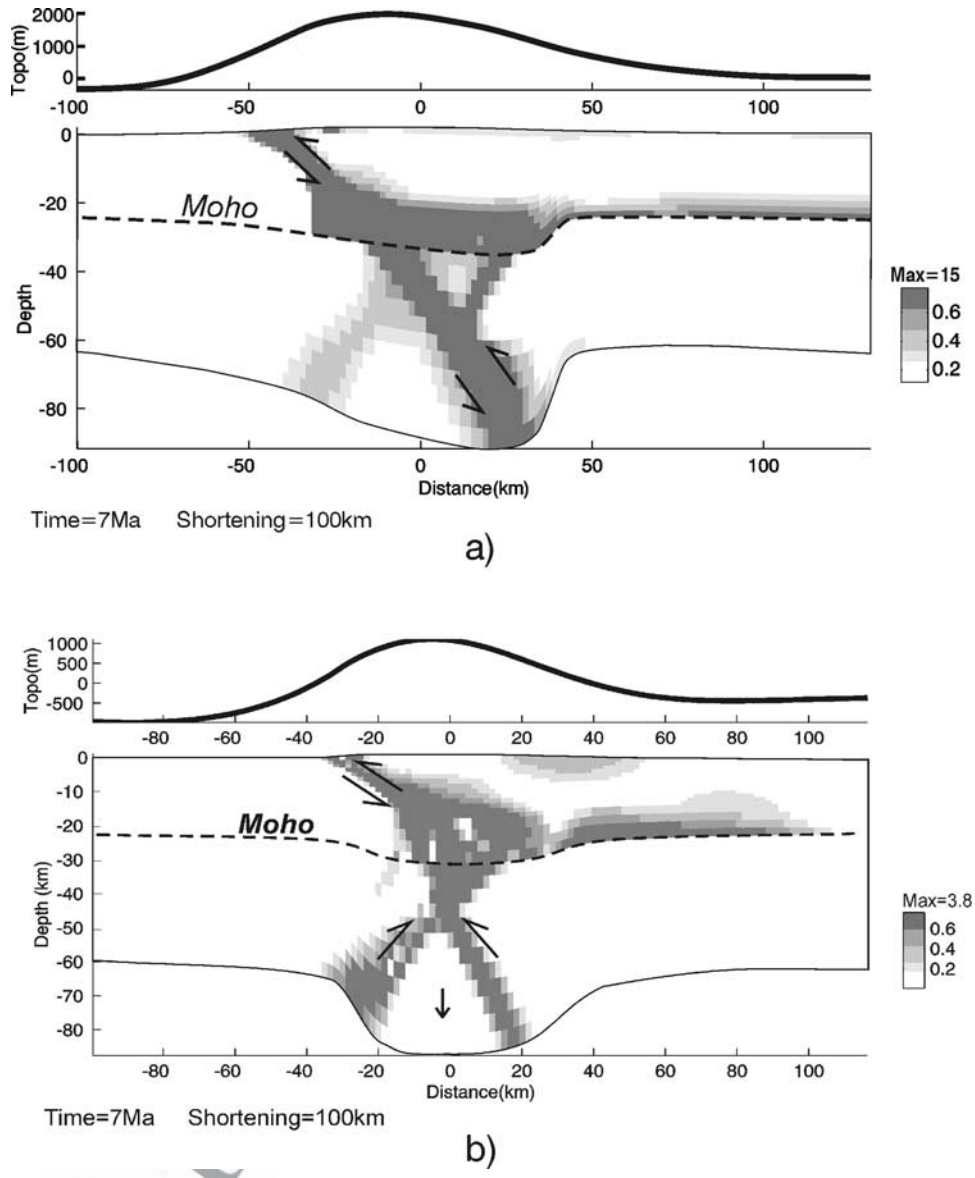

Figure 8. Models with mantle lithosphere strength of 50 MPa, reducing to 20 MPa, total shear strain (maximum in dark gray) and topography. (a) Model with strain softening in the range $\varepsilon_s = [0.01;1]$, and $k_{er} = 1000$ m^2 yr^{-1}; underthrusting of the ''Australian'' mantle. (b) Model with strain softening in the range $\varepsilon = 0.05-0.5$ and $k_{er} = 500$ m^2 yr^{-1}; symmetric thickening of the mantle lithosphere. Because the lithospheric mantle has a small strength, amplitude and wavelength of Moho deflection are small.

nesses. In contrast, if strain softening is imposed too slowly, then lithospheric thickening is too broad. In the absence of strain softening, large-scale folding of the Pacific mantle develops.

[55] Models of initial mantle strength equal to 50 MPa (Figure 8 and Table 2) illustrate the importance of strain softening on the geometry of mantle deformation. To further illustrate its effect on the width of the orogen for a stronger mantle lithosphere, Figure 9 depicts the case where strain softening is imposed more slowly than in the reference model (reduction from 200 to 50 MPa after 200% of shear strain rather than 100%, Table 2). Broad surface deformation occurs, with development of another maximum of topography located ~120 km east of the Alpine Fault zone. Shear strain propagates to the east into the ductile lower crust, and emerges to the surface via thrust faults: the secondary maximum of topography becomes as high as the primary one after 6 Myr of shortening.

4.6. Discussion of S Point Models

[56] Uniform lithospheric thickening can be approximated by considering simple elastic compressibility: results of models for a purely elastic lithosphere provide after 5 Myr and 75 km of shortening, surface uplift $y_t = 750$ m (uplift rate of 0.15 mm yr^{-1}) and bottom subsidence $y_b = 2000$ m (thickening of 4 mm yr^{-1}). By assuming a linear dependency of the vertical displacements with depth, $D(y) = y_t + (y_t - y_b)y/h_o$, the depth at which material diverges upward or downward ($D(y) = 0$) is found to be located at the midcrustal depth $S = 16.4$ km.

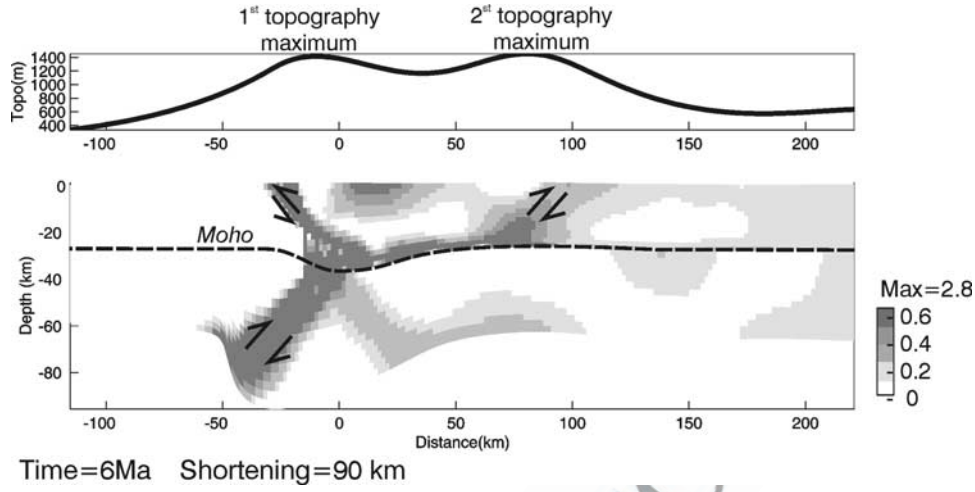

Figure 9. Model with mantle lithosphere cohesion set at 200 MPa, with slower rate of strain softening (linear decrease from 200 to 50 MPa within the range $\varepsilon_s = 0.1-2$). Deformation propagates "more" into the ductile lower crust, producing thrust faulting from $X \sim 90-130$ km. As a result, the secondary maximum of topography reaches the same height as the primary one, after only 6 Myr of shortening.

[57] Plastic and viscous behaviors trigger heterogeneous deformation that lead to continuous readjustment of the S point position, through time and space: the S point evolves within the crustal root, and would be best represented by a diffuse zone, rather than a point. Our numerical models show that the present geometry of upper crustal deformation in the Southern Alps is not very sensitive to the strength of the mantle lithosphere, because it is <200 MPa (and undergoes sufficiently rapid strain softening). In this sense, *Beaumont et al.*'s [1996] assumption of S point discontinuity at the base of the crust is a realistic approximation, as long as interest is not in the shape of the base of the crust and deeper deformation.

[58] In the present numerical models, the maximum of the topography and the deepest part of the crustal root remain on the same vertical axis (see Figure 7). The observed ~20 km offset was never satisfactorily reproduced, despite a large number of parametrical tests, including a variation of rheological properties, a varying coefficient of erosion between west and east of the Main Divide, and a tuning of strain softening coefficients. An offset of ~10 km at best was obtained when the friction angle for the Australian crust is reduced to 10°, rather than 30°. The reason for the model not producing significant offset of surface and crustal root deformation may be that only diffusive surface processes were taken into account in our models. When *Beaumont et al.* [1996, model 9] account for strain softening and asymmetric erosion processes, a significant offset is obtained [see also *Willett*, 1999]. However, we suggest that the achievement of this offset by *Beaumont et al.* [1996] is probably due to the overconstraint imposed by their basal velocity discontinuity.

[59] The observation of increasing offset of the Bouguer gravity anomaly with respect to the plate boundary, toward the southeast, where compression and surface topography decrease, indicates that this offset may find its cause in the three dimensionality of the orogen. Recent 3-D numerical modeling [*Gerbault et al.*, 2002] supports the occurrence of southward ductile lateral flow within the lower crust and along the plate boundary. Crustal thickening tends to develop toward the southeast, showing that the overall deformation results from a tendency to equilibrate buoyancy forces in both the vertical section and laterally, according to pressure variations. This thickening results from the geometry of rheological discontinuities with respect to the orientation of the relative plate velocity vector, and coincides with the shape of the Bouguer anomaly.

5. Conclusion

[60] Our numerical models involve compression of the entire continental lithosphere during the first 10 Myr of orogenic growth. While the models presented are nonunique, they are, nonetheless, the culmination of a number of tests that provide a mechanism explaining within a single self-consistent geodynamical framework to compare with crustal deformation data from the Southern Alps of New Zealand (surface structures, GPS, electrical conductivity, seismic velocities). The modeling also demonstrates the importance of the strength of the lithospheric mantle on the geometry of the collision process.

[61] 1. Advection appears to be the main mechanism that accounts for the deflection/uplift of isotherms after 7 Myr of shortening (Figure 4b). This confirms the validity of the thermokinematical approach of *Shi et al.* [1996].

[62] 2. Crustal deformation is characterized by a major shear zone that one can associate with the Alpine Fault, which from being initially vertical, inclines to ~45° and curves at depth to merge with a ductile shear in the lower crust (Figure 4e). This illustrates the inclination through time of an initially vertical transcurrent shear zone, and is consistent with 3-D modeling [*Gerbault et al.*, 2002].

[63] 3. Flexure of the brittle upper crust above the crustal root is responsible for faulting being concentrated 60–80 km east from the Alpine Fault (Figure 5) and is coincident with several active faults and with the boundary of the observed U-shaped electrical conductor [*Wannamaker et al.*, 2002]. The argument that midcrustal fluids accumulate in a locally

extended zone (less compressed) in the lower crust and then migrate to the surface finds further support here in our dynamical modeling.

[64] 4. Comparison with GPS data of horizontal convergence velocity shows that the change in slope at a distance of 80–100 km from the Alpine Fault can be related to the place where the upper crust detaches from the mantle lithosphere (Figures 5 and 6). The increase in velocity at the Alpine Fault, in the model, is sharper than in GPS data, because geodetic measurements account for short timescale aseismic deformation.

[65] 5. As compression increases, flow in the ductile lower crust propagates to the east, so that the upper crust detaches from the lithospheric mantle. The tip of this ductile shear zone, located ~100–130 km from the Alpine Fault, can connect to thrust faults in the upper crust, and generate surface uplift. This characteristic distance and the amount of surface uplift associated with it are not only dependent on the (low) strength of the ductile lower crust but also on the high strength of the lithospheric mantle (200 MPa). The occurrence of mantle earthquakes beneath the South Island may be controlled by large shear strain associated with mantle subduction. In addition, the large strain modeled in the crust and lithospheric mantle under the Southern Alps may also generate heterogeneity that could be manifested as seismic anisotropy.

[66] 6. The crustal root develops and resembles the image obtained from seismic velocity models in the central Southern Alps, with ''subduction of Pacific'' mantle. If the strength of the lithospheric mantle is weaker than 200 MPa, the amplitude and wavelength of the crustal root are too small (Figure 8). If the rate of softening is too slow then the resulting surface deformation is too broad (Figure 9); a result that was also demonstrated by *Pysklywec et al.* [2000, 2002]. Satisfactory models with softening ranging from 200 to 50 MPa are consistent with a number of geophysical studies that estimated maximum stress contrast that a lithosphere can support [e.g., *McNutt*, 1980; *Molnar and England*, 1990; *Gerbault*, 2000]. The typical horizontal integrated force in our models is $2–6\ 10^{12}$ N m.

[67] 7. A satisfactory fit is obtained to the measured gravity anomaly for our reference model, without needing to account for denser mantle lithosphere [*Stern*, 1995; *Stern et al.*, 2000]. This difference, however, warrants further investigation. The lithosphere-asthenosphere boundary in our models was taken as a basal boundary condition, and modeling the full dynamics of this zone requires extending our initial model to greater depth (at least 120 km). While numerical modeling such as that of *Pysklywec et al.* [2000, 2002] or *Arnold et al.* [2001] addresses the possible modes of deformation at depths corresponding to the lithosphere-asthenosphere boundary, there is still a lot to learn from worldwide variations in density, elastic parameters, and viscosity at these depths [e.g., *Karato*, 1993; *Ishii and Tromp*, 1999; *Petrini et al.*, 2001; *Sabadini et al.*, 2002]. In relation to this, an appropriate constitutive law for the upper mantle is still missing, while modeling confirms its control on the (a)symmetry of deformation (e.g., strain softening of *Huismans and Beaumont* [2002]). Our modeling indicates that for the Southern Alps, an asymmetric crustal root but symmetric lithosphere thickening would require more complex constitutive laws than those used here.

[68] 8. The 20 km offset between the maximum topography and maximum depth of the crustal root were not reproduced in the models, despite a number of parametric tests. Because the observed Bouguer gravity low increases progressively to the southeast and away from the plate boundary, indicating that deep crustal thickening does not strike parallel to the plate boundary, we suggest that the dynamic equilibrium of the orogen is three dimensional. Although many of the observed deformational structures at an obliquely converging zone like the Southern Alps may be modeled using 2-D orthogonal compression, structures that do not strikeparallel require 3-D modeling.

[69] Finally, here we modeled the first stage of mountain growth, also called the linear growth stage [e.g., *Shen et al.*, 2001]. At times greater than 10 Myr, several studies emphasize the role of ductile, channel flow in the lower crust in monitoring the lateral expansion of the orogen [*Royden*, 1996; *Vanderhaeghe et al.*, 1999]. In our models, the change in shear direction within the ductile lower crust (see Figure 5) illustrates the complexity of ductile flow processes at the edge of a continental orogen, in its initial stages.

Appendix A: Numerical Method

[70] Algorithm Parovoz [*Poliakov and Podladchikov*, 1992] belongs to the fast Lagrangian analysis of continua (FLAC) family [*Cundall and Board*, 1988; *Cundall*, 1989], which is a large-strain fully explicit time-marching numerical algorithm exploiting the Lagrangian moving grid method. The latter allows for solution of Newton's equation of motion in large strain mode, holding a locally symmetric small strain formulation commonly used in continuum mechanics. The method can reproduce initialization and evolution of nonpredefined faults (treated as large shear bands).

[71] The time-marching scheme of the algorithm means that one loop represents one time step, which must be small enough to prevent the physical information propagating from one element to its neighbor during this interval of time. Each loop contains the following procedure: velocities are calculated from Newton's law, with density ρ, time t, velocity vector v, and gravity acceleration g:

$$\rho \delta v_i / \delta t = \delta \sigma_{ij} / \delta x_j + \rho g.$$

Components for the deformation rate are deduced from $\varepsilon_{ij} = 1/2\ (\delta v_i/\delta x_j + \delta v_j/\delta x_i)$.

[72] Brittle-elastic-viscous constitutive laws then provide the stress distribution and equivalent forces $\rho \delta v_i/\delta t$, which in turn provide input for the next time step. The algorithm employs a dynamic relaxation technique based on the introduction of artificial masses in the dynamic system, permitting to handle strain localization. The adaptive remeshing technique allows the models to be run up to ~25% of total shortening.

[73] Brittle-elastic-viscous behavior is modeled so that the minimum deviatoric stress produced by Mohr-Coulomb elastoplasticity and Maxwell viscoelasticity is retained, at each time step and for each element. Thus the brittle-ductile transition is self-defined in the model and is referred to as the depth at which the deviatoric shear stress becomes lower

than ~20 MPa, regardless of which brittle or ductile behavior actually dominates [e.g., *Rannali*, 1995]. The failure criterion is reached when the relationship between normal and tangential stresses, σ_n and τ, along any given orientation equals $\tau = S_o - \tan\phi\sigma_n$, S_o being the cohesion and ϕ the friction angle for a given material property. Dilatancy angle $\psi = 0$, so that nonassociated plasticity occurs [see *Vermeer*, 1990].

[74] Viscous behavior is prescribed by power law dislocation creep, and *Chen and Morgan's* [1990] expression of the effective viscosity is used, with Q the activation energy, R the gas constant, A the material constant, and T the absolute temperature (see text for definitions of σ_s and ε_s):

$$\mu^* = 1/4[4/(3A)]^{1/n}\varepsilon_s^{1/n-1}\exp(Q/nRt) = \sigma_s/2\varepsilon_s.$$

When the stresses are evaluated, the increase in strain rate is greater than the decrease in effective viscosity, so that the shear stress actually increases in a shear zone. For this reason, in the Pacific crust, we introduce softening of the viscosity by a factor 10 within a certain range of the total shear strain ε_s (see Table 1).

[75] Extrapolation of the power law creep parameters for olivine in the upper mantle lithosphere may provide greater shear stress than the Mohr-Coulomb yield stress. Since dominant deformation processes at mantle depth are poorly known, a number of studies then assume a brittle behavior [see *Ranalli*, 1995; *Burov and Diament*, 1995]. For this reason, we chose to empirically assign zero friction and test the cohesion for the mantle lithosphere. Also, we test cohesion strain softening of the mantle lithosphere, as it appears necessary to allow for localized thickening (see Table 1 for parameters and section 4.3). *Pysklywec et al.* [2002], for example, apply friction strain softening. Cohesion or friction strain softening is achieved by reducing their value according to a linear equation that depends on the amount of total shear strain (see Table 1). Softening of friction angle in the Australian crust is introduced to allow deformation to propagate to the right of the modeled plate boundary, and allows the maximum of topography to develop to the right of the thickened crust. Softening of the viscosity of the Pacific crust allows the deformation to remain localized close to the plate boundary.

[76] Temperature is updated through time. The heat flux through an element of volume is equal to the heat produced by internal sources plus the variation of volume. If heat is advected with velocity V_i, H is the heat production per unit mass, k is the thermal diffusivity, and ρ is the density, the general equation of heat is [*Ranalli*, 1995]

$$\partial T/\partial t + V_i\nabla T - k\nabla^2 T = \rho H.$$

The initial continental temperature field is calculated according to the age-dependent procedure developed by *Burov and Diament* [1995], with a crustal heat production $H = H_s \exp -y/h_r$), and $H_s = 9 \times 10^{-10}$ W kg^{-1}, $h_r = 10$ km, and crust and mantle thermal conductivities $\kappa_c = \kappa_m = 3$ W K^{-1} m^{-1} ($\kappa = k\rho C_p$, $C_p = 1$ kJ kg^{-1} K^{-1} the specific heat). For a lithosphere of thermal age of 100 Ma, a temperature $T_b = 1350$°C at the base of the lithosphere $h_l = 60$ km, the resulting geotherm leads to the 600°C isotherm lying at ~25 km depth. After 7 Myr of shortening, the far-field surface heat flux is ~60 mW m^{-1} K^{-1}, increasing to ~120 mW m^{-1} K^{-1} at the topography maximum.

[77] Erosion and sedimentation processes are taken into account with a classic equation of diffusion. The equation of mass conservation is written in terms of a linear relationship between the variation of surface elevation h with time and the surface slope derivative. We adopt a constant value for the coefficient of diffusion k_{er} (set to 1000 m^2 yr^{-1}), so that $\partial h/\partial t = k_{er}\partial^2 h/\partial x^2$. If the area of an element increases by more than half of its initial value, then the element's "phase" switches to a "sediment" rheology (Table 1).

[78] The Bouguer gravity anomaly is modeled from the progressive displacement of layers since time 0 when the model is assumed to be in equilibrium with no anomaly. The gravity anomaly relates to the vertical displacement dz of element (i) of width dx located at the boundary between layers of different density $\Delta\rho$. Element (i) contributes to the gravity anomaly by $dg_i = 2G\,\Delta\rho\,dx\,dz$, where the gravitational constant $G = 6.67 \times 10^{-11}$ m^3 kg^{-1} s^{-2}.

[79] Each element (k) at the surface of the model is thus subjected to anomalous gravity acceleration created by the displacement of elements (i) that compose the layer boundary (l) of contrasted density. Three layers (l) of contrasted density exist: the upper and lower crust boundary ($\Delta\rho = 250$ kg m^{-3}), the crust and the mantle boundary at the Moho ($\Delta\rho = 300$ kg m^{-3}), and the base of the model ($\Delta\rho = 50$ kg m^{-3}). For elements (i) at depth z_i, located on (l), and with r_i the distance between (k) and (i):

$$gb(k) = \Sigma_l\Sigma_i(dg_i\,z_i)/r_i^2.$$

[80] **Acknowledgments.** S. Cox, R. Sutherland, D. Woodward, D. Eberhart-Phillips, M. McSaveney, P. Koons, P. Upton, G. Caldwell, and M. Scherwath provided extended information on the Southern Alps geology and geophysics. S. Ellis, D. Woodward, and J. Beavan provided useful comments on the manuscript. We also thank R. Pysklywec, T. Stern, and J. Braun for their thorough reviews. This study was funded by New Zealand Foundation for Research, Science and Technology (contract 05X0010) provided to the Institute of Geological and Nuclear Sciences (contribution 2222). Vrije Universiteit in Amsterdam has kindly provided facilities for M.G. to continue working on this project.

References

Adams, C. J., and J. E. Gabites, Age of metamorphism and uplift of the Haast schist Group at Haast Pass, Lake Wanaka and Lake Hawea, South Island, New Zealand, *N. Z. J. Geol. Geophys.*, *28*, 85–96, 1985.

Arnold, J., W. R. Jacoby, H. Schmeling, and B. Schott, Continental collision and the dynamic and thermal evolution of the Variscan orogenic crustal root—Numerical models, *J. Geodyn.*, *31*, 273–291, 2001.

Batt, G. E., and J. Braun, The tectonic evolution of the Southern Alps, New Zealand: Insights from fully thermally coupled dynamical modeling, *Geophys. J. Int.*, *136*, 403–420, 1999.

Beanland, S., Field guide to sites of active Earth deformation, South Island, New Zealand, 104 pp., N. Z. Geol. Surv., Lower Hutt, New Zealand, 1987.

Beaumont, C., P. Fullsack, and J. Hamilton, Erosional control of active compressional orogens, in *Thrust Tectonics*, edited by K. R. McClay, pp. 1–18, Chapman and Hall, New York, 1992.

Beaumont, C., P. J. Kamp, J. Hamilton, and P. Fullsack, The continental collision zone South Island, New Zealand: Comparison of geodynamical models and observations, *J. Geophys. Res.*, *101*, 3333–3359, 1996.

Beavan, J., and J. Haines, Contemporary horizontal velocity and strain-rate fields of the Pacific-Australian plate boundary zone through New Zealand, *J. Geophys. Res.*, *106*, 741–770, 2001.

Brace, W. F., and D. L. Kohlstedt, Limits on lithospheric stress imposed by laboratory experiments, *J. Geophys. Res.*, *85*, 6248–6252, 1980.

Braun, J., and C. Beaumont, Three dimensional numerical experiments of strain partitioning at oblique plate boundaries: Implications for contrasting tectonic styles in California and South Island, New Zealand, *J. Geophys. Res.*, *100*, 18,059–18,074, 1995.

Buck, W. R., and A. N. B. Poliakov, Abyssal hills formed by stretching oceanic lithosphere, *Nature*, *392*, 272–275, 1998.

Bull, J. M., J. Martinod, and P. Davy, Buckling of the oceanic lithosphere from geophysical data and experiments, *Tectonics*, *11*, 537–548, 1992.

Burg, J. P., and Y. Podladchikov, Lithospheric scale folding; numerical modeling and application to the Himalayan syntaxes, *Int. J. Earth Sci.*, *88*(2), 190–200, 1999.

Burov, E. B., and M. Diament, The effective elastic thickness of continental lithosphere: What does it really mean?, *J. Geophys. Res.*, *100*, 3905–3927, 1995.

Burov, E. B., and A. Poliakov, Erosion and rheology controls on synrift and postrift evolution: Verifying old and new ideas using a fully coupled numerical model, *J. Geophys. Res.*, *106*, 16,461–16,481, 2001.

Burov, E. B., L. I. Lobkovsky, S. Cloetingh, and A. M. Nikishin, Continental lithosphere folding in central Asia (II): Constraints from gravity and topography, *Tectonophysics*, *226*, 73–87, 1993.

Carter, R. M., and R. J. Norris, Cenozoic history of southern New Zealand: An accord between geological observations and plate-tectonic predictions, *Earth Planet. Sci. Lett.*, *31*, 85–94, 1976.

Chen, Y., and W. J. Morgan, A nonlinear rheology model for mid-ocean ridge axis topography, *J. Geophys. Res.*, *95*, 17,583–17,604, 1990.

Cloetingh, S., E. Burov, and A. Poliakov, Lithosphere folding: Primary response to compression? (from central Asia to Paris Basin), *Tectonics*, *18*, 1064–1083, 1999.

Cox, S. C., and R. H. Findlay, The Main Divide fault zone and its role in the formation of the Southern Alps, New Zealand, *N. Z. J. Geol. Geophys.*, *38*, 489–501, 1995.

Cundall, P. A., Numerical experiments on localization in frictional materials, *Ing. Arch.*, *59*, 148–159, 1989.

Cundall, P., and M. Board, A microcomputer program for modeling large-strain plasticity problems, *Numer. Methods Geomech.*, *6*, 2101–2108, 1988.

Davey, F. J., et al., Preliminary results from a geophysical study across a modern, continent-continent collisional plate boundary-The Southern Alps, New Zealand, *Tectonophysics*, *288*, 221–235, 1998.

DeMets, C., R. G. Gordon, D. F. Argus, and S. Stein, Current plate motions, *Geophys. J. Int.*, *101*, 425–478, 1990.

Eberhart-Phillips, D., and S. Bannister, Three-dimensional crustal structure in the Southern Alps region of New Zealand from inversion of local earthquake and active source data, *J. Geophys. Res.*, *107*(B10), 2262, doi:10.1029/2001JB000567, 2002.

Field, B. D., and G. H. Browne, Cretaceous and Cenozoic sedimentary basins and geological evolution of the Canterbury Region, South Island, New Zealand, *Basin Stud. 2*, 94 pp., Inst. of Geol. and Nucl. Sci., Lower Hutt, 1989.

Gerbault, M., At what stress level is the Indian Ocean lithosphere buckling?, *Earth Planet. Sci. Lett.*, *178*, 165–181, 2000.

Gerbault, M., A. N. B. Poliakov, and M. Daignières, Prediction of faulting from the theories of elasticity and plasticity, what are the limits?, *J. Struct. Geol.*, *20*, 301–320, 1998.

Gerbault, M., E. B. Burov, A. N. B. Poliakov, and M. Daignières, Do faults trigger folding in the lithosphere?, *Geophys. Res. Lett.*, *26*, 271–274, 1999.

Gerbault, M., F. Davey, and S. Henrys, Three-dimensional lateral crustal thickening in continental oblique collision: An example from the Southern Alps, New Zealand, *Geophys. J. Int.*, *150*, 770–779, 2002.

Godfrey, N. J., F. Davey, T. A. Stern, and D. Okaya, Crustal structure and thermal anomalies of the Dunedin Region, South Island, New Zealand, *J. Geophys. Res.*, *106*, 30,835–30,848, 2001.

Griffiths, G. A., and M. J. McSaveney, Distribution of mean annual precipitation across some steepland regions of New Zealand, *N. Z. J. Sci.*, *26*, 197–209, 1983.

Houseman, G. A., D. P. McKenzie, and P. Molnar, Convective instability of a thickened boundary layer and its relevance for the thermal evolution of continental convergence belts, *J. Geophys. Res.*, *86*, 6115–6132, 1981.

Huismans, R. S., and C. Beaumont, Asymmetric lithospheric extension: The role of frictional plastic strain softening inferred from numerical experiments, *Geology*, *30*, 211–214, 2002.

Ishii, M., and J. Tromp, Normal-mode and free-air gravity constraints on lateral variations in velocity and density of the Earth's mantle, *Science*, *285*, 1231–1236, 1999.

Karato, S.-I., Importance of anelasticity in the interpretation of seismic tomography, *Geophys. Res. Lett.*, *20*, 1623–1626, 1993.

Kohler, M., and D. Eberhart-Phillips, Three-dimensional lithospheric structure below the South Island of New Zealand, *J. Geophys. Res.*, *107*(B10), 2225, doi:10.1029/2001JB000182, 2002.

Koons, P. O., The topographic evolution of collisional mountain belts: A numerical look at the Southern Alps, New Zealand, *Am. J. Sci.*, *289*, 1041–1069, 1989.

Koons, P. O., Two-sided orogen: Collision and erosion from the sandbox to the Southern Alps, New Zealand, *Geology*, *18*(8), 679–682, 1990.

Koons, P. O., and C. M. Henderson, Geodetic analysis of model oblique collision and comparison to the Southern Alps of New Zealand, *N. Z. J. Geol. Geophys.*, *38*(4), 545–552, 1995.

Laird, M. G., Cretaceous continental rifts: New Zealand region, in *Sedimentary Basins of the World*, vol. 2, *South Pacific Sedimentary Basins*, edited by P. F. Balance, pp. 37–49, Elsevier Sci., New York, 1993.

Leitner, B., D. Eberhart-Phillips, H. Anderson, and J. L. Nabelek, A focused look at the Alpine Fault, New Zealand, focal mechanisms and stress observations, *J. Geophys. Res.*, *106*, 2193–2220, 2001.

Little, T. A., R. J. Holcombe, and B. R. Ilg, Kinematics of oblique continental collision inferred from ductile microstructures and strain in mid-crustal Alpine Schist, central South Island, New Zealand, *J. Struct. Geol.*, *24*, 219–239, 2001.

Long, D., S. C. Cox, S. Bannister, M. C. Gerstenberger, and D. Okaya, Upper crustal structure beneath the eastern Southern Alps and the Mackezie basin, New Zealand, derived from seismic reflection data, *N. Z. J. Geol. Geophys.*, *46*, 21–39, 2003.

Martinod, J., and P. Davy, Periodic instabilities during compression of the lithosphere: 1. Deformation modes from an analytical perturbation method, *J. Geophys. Res.*, *97*, 1999–2014, 1992.

Mattauer, M., Intracontinental subduction, crust-mantle décollement and crustal-stacking wedge in the Himalayas and other collision belts, in *Collision Tectonics*, edited by M. P. Coward and A. C. Ries, *Geol. Soc. Spec. Publ.*, *19*, 37–50, 1986.

McNutt, M., Implications of regional gravity for state of stress in the Earth's crust and upper mantle, *J. Geophys. Res.*, *85*, 6377–6396, 1980.

Molnar, P., and P. England, Temperatures, heat flux, and frictional stress near major thrust faults, *J. Geophys. Res.*, *95*, 4833–4856, 1990.

Molnar, P., et al., Continuous deformation versus faulting through the continental lithosphere of New Zealand, *Science*, *286*, 516–519, 1999.

Moore, M., P. England, and B. Parsons, Relation between surface velocity field and shear wave splitting in the South Island of New Zealand, *J. Geophys. Res.*, *107*(B9), 2198, doi:10.1029/2000JB000093, 2002.

Mortimer, N., Basement geology of South Island of New Zealand, paper presented at IGNS Conference, Inst. of Geol. and Nucl. Sci., Wellington, 2000.

Oliver, P. J., and H. W. Keene, Clearwater, Geological map of New Zealand, scale 1:50000, sheet J36D and part sheet J35, map (1 sheet) and notes (48 pp.), Dep. of Sci. and Ind. Res., Wellington, 1990.

Petrini, K., A. D. Connoly, and Y. Y. Podladchikov, A coupled petrological-tectonic model for sedimentary basin evolution: The influence of metamorphic reactions on basin subsidence, *Terra Nova*, *13*, 354–359, 2001.

Poliakov, A., and Y. Podladchikov, Diapirism and topography, *Geophys. J. Int.*, *109*, 553–564, 1992.

Pysklywec, R. N., C. Beaumont, and P. Fullsack, Modeling the behaviour of the continental mantle lithosphere during plate convergence, *Geology*, *28*, 655–658, 2000.

Pysklywec, R. N., C. Beaumont, and P. Fullsack, Lithospheric deformation during the early stages of continental collision: Numerical experiments and comparison with South Island, New Zealand, *J. Geophys. Res.*, *107*(B7), doi:10.1029/2001JB000252, 2002.

Ranalli, G., *Rheology of the Earth*, 2nd ed., 413 pp., Chapman and Hall, New York, 1995.

Reyners, M., Subcrustal earthquakes in the central south Island, New Zealand, and the root of the Southern Alps, *Geology*, *15*, 1168–1171, 1987.

Royden, L. H., Coupling and decoupling of crust and mantle in convergent orogens: Implications for strain partitioning in the crust, *J. Geophys. Res.*, *101*, 17,679–17,705, 1996.

Sabadini, R., A. M. Marotta, R. De Franco, and L. L. A. Vermeersen, Style of density stratification in the mantle and true polar wander induced by ice loading, *J. Geophys. Res.*, *107*(B10), 2258, doi:10.1029/2001JB000889, 2002.

Scherwath, M., Crustal structure of the central South Island, New Zealand from an onshore-offshore seismic data, thesis, Victoria Univ. of Wellington, 2001.

Scherwath, M., T. Stern, D. Okaya, R. Daview, S. Kleffmann, and F. Davey, Crustal structure from seismic data in the vicinity of the Alpine Fault, New Zealand, results from SIGHT line 2, *Eos Trans. AGU*, *79*(45), Fall Meet. Suppl., F901, 1998.

Scherwath, M., T. A. Stern, R. A. Davies, F. J. Davey, D. A. Okaya, and S. Kleffmann, Crustal structure and lithospheric deformation within a continental collision zone, South Island, New Zealand, *Eos Trans. AGU*, *81*(48), Fall Meet. Suppl., Abstract T22A-13, 2000.

Shen, F., L.-H. Royden, and B.-C. Burchfiel, Large-scale crustal deformation of the Tibetan Plateau, *J. Geophys. Res.*, *106*, 6793–6816, 2001.

Shi, Y., R. Allis, and F. Davey, Thermal modeling of the Southern Alps, New Zealand, *Pure Appl. Geophys.*, *146*, 469–501, 1996.
Sircompe, K. N., and P. J. Kamp, The South Westland Basin; seismic stratigraphy, basin geometry and evolution of a foreland basin within the Southern Alps collision zone, New Zealand, *Tectonophysics*, *300*, 359–387, 1998.
Stern, T., Gravity anomalies and crustal loading at and adjacent to the Alpine Fault, New Zealand, *N. Z. J. Geol. Geophys.*, *38*, 593–600, 1995.
Stern, T., P. Molnar, D. Okaya, and D. Eberhart-Phillips, eleseismic *P* wave delays and modes of shortening the mantle lithosphere beneath South Island, New Zealand, *J. Geophys. Res.*, *105*, 21,615–21,631, 2000.
Stern, T., S. Kleffmann, D. Okaya, M. Scherwath, and S. Bannister, Low seismic-wave speeds and enhanced fluid pressure beneath the Southern Alps of New Zealand, *Geology*, *29*, 679–682, 2001.
Sutherland, R., F. Davey, and J. Beavan, Plate boundary deformation in South Island, New Zealand, is related to inherited lithospheric structure, *Earth Planet. Sci. Lett.*, *177*, 141–151, 2000.
Templeton, A. S., C. P. Chamberlain, P. O. Koons, and D. Craw, Stable isotopic evidence for mixing between metamorphic fluids and surface-derived waters during recent uplift in the Southern Alps of New Zealand, *Earth Planet. Sci. Lett.*, *154*, 73–92, 1998.
Tippett, J.-M., and P. Kamp, Fission track analysis of the late Cenozoic vertical kinematics of continental Pacific crust, South Island, New Zealand, *J. Geophys. Res.*, *98*, 16,119–16,148, 1993.
Tullis, J., and R. A. Yund, Diffusion creep in feldspar aggregates: Experimental evidence, *J. Struct. Geol.*, *13*, 987–1000, 1991.
Vacher, P., and A. Souriau, A three-dimensional model of the Pyrenean deep structure based on gravity modeling, seismic images and petrological constraints, *Geophys. J. Int.*, *145*, 460–470, 2001.
Vanderhaeghe, O., C. Beaumont, P. Fullsack, and R. Jamieson, Role of partial melting during orogenic evolution; insights from thermomechanical modeling, *J. Conf. Abstr.*, *4*, 426, 1999.
Vermeer, P. A., The orientation of shear bands in biaxial tests, *Géotechnique*, *40*, 223–236, 1990.
Walcott, R. I., Modes of oblique compression: Late Cenozoic Tectonics of the South Island of New Zealand, *Rev. Geophys.*, *36*, 1–26, 1998.
Wannamaker, P. E., G. R. Jiracek, J. A. Stodt, T. G. Caldwell, V. M. Gonzalez, J. D. McKnight, and A. D. Porter, Fluid generation and pathways beneath an active compressional orogen, the New Zealand Southern Alps, inferred from magnetotelluric data, *J. Geophys. Res.*, *107*(B6), 2117, doi:10.1029/2001JB000186, 2002.
Wellman, H. W., An uplift map for the South Island of New Zealand, and a model for uplift of the Southern Alps, *Bull. R. Soc. N. Z.*, *18*, 13–20, 1979.
Wellman, H. W., and R. W. Willet, The geology of the west coast from Abut Head to Milford sound, part 1, *Trans. R. Soc. N. Z.*, *71*, 282–306, 1942.
Willett, S. D., Orography and orogeny: The effects of erosion on the structure of mountain belts, *J. Geophys. Res.*, *104*, 28,957–28,981, 1999.
Woodward, D. J., The crustal structure of the Southern Alps, New Zealand, as determined by gravity, in *The Origin of the Southern Alps*, edited by R. I. Walcott and M. M. Cresswell, *Bull. R. Soc. N. Z.*, *18*, 95–98, 1979.
Woodward, D. J., F. J. Davey, and J. M. Ravens, Seismic tests for the South Island Transect 1993, *Rep. 94/31*, 17 pp., Inst. of Geol.and Nucl. Sci., Lower Hutt, 1994.
Zhang, S., S. I. Karato, G. J. Fitz, U. H. Faul, and Y. Shou, Simple shear deformation of olivine aggregates, *Tectonophysics*, *316*, 133–152, 2000.

F. Davey and S. Henrys, Geological and Nuclear Sciences, Gracefield, PO Box 30-368 Lower Hutt, New Zealand.
M. Gerbault, IRD UR 104, Univ. é P. Sabatier, 38 rue des 36-ponts, F-31400 Toulouse, France. (gerbault@lmtg.ups-tlse.fr)